NANO LETTERS

Letter

pubs.acs.org/NanoLett

Real-Space Mapping of the Chiral Near-Field Distributions in Spiral Antennas and Planar Metasurfaces

M. Schnell,[†] P. Sarriugarte,[†] T. Neuman,[‡] A. B. Khanikaev,[§] G. Shvets,[∥] J. Aizpurua,[‡] and R. Hillenbrand*[,⊥,#]

[†]CIC nanoGUNE, 20018 Donostia − San Sebastián, Spain

[‡]Centro de Fisica de Materiales CSIC-UPV/EHU and Donostia International Physics Center DIPC, 20018 Donostia − San Sebastián, Spain

[§]Department of Physics, Queens College and Graduate Center of The City University of New York, New York, NewYork, 11367, United States

[∥]Department of Physics, The University of Texas at Austin, Austin, Texas 78712, United States

[⊥]CIC nanoGUNE and EHU/UPV, 20018 Donostia − San Sebastián, Spain

[#]IKERBASQUE, Basque Foundation for Science, 48011 Bilbao, Spain

Supporting Information

ABSTRACT: Chiral antennas and metasurfaces can be designed to react differently to left- and right-handed circularly polarized light, which enables novel optical properties such as giant optical activity and negative refraction. Here, we demonstrate that the underlying chiral near-field distributions can be directly mapped with scattering-type scanning near-field optical microscopy employing circularly polarized illumination. We apply our technique to visualize, for the first time, the circular-polarization selective nanofocusing of infrared light in Archimedean spiral antennas, and explain this chiral optical effect by directional launching of traveling waves in analogy to antenna theory. Moreover, we near-field image single-layer rosette and asymmetric dipole−monopole metasurfaces and find negligible and strong chiral optical near-field contrast, respectively. Our technique paves the way for near-field characterization of optical chirality in metal nanostructures, which will be essential for the future development of chiral antennas and metasurfaces and their applications.

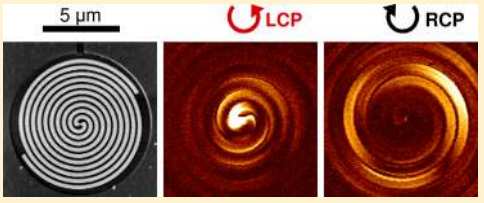

KEYWORDS: *Optical antennas, metasurfaces, SNOM, near-field microscopy, plasmonics, optical chirality*

Optical antennas[1] and metamaterials[2,3] allow for fascinating new ways of manipulating light far beyond the capabilities of classical optical components, which has paved the way to novel photonic applications ranging from ultrasensitive spectroscopy[4,5] and ultrafast photodetectors[6] to negative refraction[7,8] and perfect absorption.[9] Recently, a significant research interest was found with chiral metal nanostructures, where the individual elements or their arrangement have the property of handedness.[2,10−25] They exhibit a different optical response to left (LCP) and right circularly polarized (RCP) light, which can be engineered to be much stronger than that of natural materials such as chiral (bio)molecules. This chiral optical effect can be exploited to produce an extraordinarily large optical activity and circular dichroism (CD) in chiral metamaterials, which may be used for broadband circular polarizers,[16,21] or to achieve negative refraction based on a chiral resonance.[15,19,23] Furthermore, optical chirality can be strongly enhanced in the vicinity of chiral antennas, enabling novel CD spectroscopy applications with greatly improved sensitivity for the molecules' handedness.[10,20,25,26]

Interestingly, chirality is also found in radiofrequency antenna design such as with helical and spiral antennas,[27−29] where the chiral antenna geometry provides radiation with circular polarization, thus offering improved radio transmission in situations where the relative orientation of transmitting and receiving antennas is unknown or multipath interferences occur. First studies have demonstrated functional optical and infrared spiral antennas and have investigated their radiation properties in the far field as well as reception of thermal radiation.[30−33] However, transmission and reception with circular polarization, and particularly the chiral near-field response, are widely unexplored.

So far, experimental characterization of optical chirality is mainly based on far-field spectroscopy,[11−22] which however provides only limited information on the underlying microscopic mechanisms. For example, while optical activity and circular dichroism of metal nanostructures can be directly measured in transmission experiments, its root cause, the surface charge and current distributions, cannot be experimentally confirmed. Nanoimaging techniques are thus needed to verify theoretically predicted surface charge distributions and

Received: October 30, 2015
Revised: December 7, 2015
Published: December 14, 2015

DOI: 10.1021/acs.nanolett.5b04416
Nano Lett. 2016, 16, 663−670

to test real-world structures in the near field. The latter is particularly important for control and optimization of the fabrication process because the chiral optical response critically depends on absorption losses in the metal structures,[34−38] the actual element shape and the quality of interelement alignment.[13] In first studies, the near-field distributions in chiral antennas and metasurfaces were mapped with near-field microscopy employing linearly polarized illumination,[39] and also maps of the differential near-field signal for periodically changing LCP and RCP excitation were obtained.[40,41] However, the near-field distributions in antennas and metasurfaces excited by circularly polarized light, the relevant polarization in dichroism measurements and chiral negative refraction, have not been imaged yet.

Here we demonstrate that the chiral near-field distributions in extended two-dimensional nanostructures can be mapped directly and in real space with scattering-type scanning near-field optical microscopy (s-SNOM)[42−52] employing circularly polarized illumination. We apply our technique to provide experimental evidence of the circular-polarization-sensitive nanofocusing capabilities of infrared Archimedean spiral nanoantennas in the near field, as a canonical example of chiral antenna structures. We also investigate how the circular polarization contrast depends on the antenna arm length and explain the findings in terms of standing wave and traveling wave concepts from antenna theory. We furthermore apply our technique to image the chiral near-field distributions of a single-layer rosette metasurface and an asymmetric dipole−monopole metasurfaces[36] and connect the results with the chiral optical response (circular dichroism) in the far field.

In Figure 1, we introduce and illustrate s-SNOM antenna mapping employing circularly polarized light. Our setup is

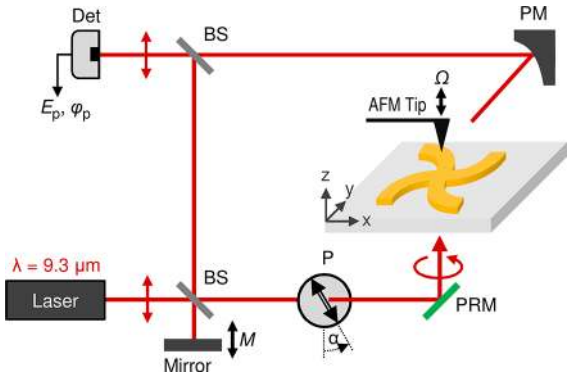

Figure 1. Transmission-mode s-SNOM for near-field mapping with circularly polarized illumination. Laser, CO_2 laser emitting at 9.3 μm wavelength; BS, beam splitter; P, linear polarizer; PRM, infrared phase retarding mirror; AFM, atomic force microscope; PM, parabolic mirror; Det, pseudoheterodyne detection.

based on transmission-mode s-SNOM.[42−44] The sample is illuminated from below at normal incidence with a weakly focused laser beam at a wavelength of 9.3 μm with left- (LCP) or right-handed circular polarization (RCP), see Methods for details. While scanning the sample, a sharp dielectric tip locally scatters the near fields on the sample surface. The p-component of the scattered light from the tip and the sample is recorded with a pseudoheterodyne interferometer, yielding the near-field amplitude and phase images, $|E_p|$ and φ_p.

Typically, the experimental near-field images ($|E_p|$, φ_p) have been compared to the z-component of the calculated near-field distribution ($|E_z|$, φ_z). However, a recent study has revealed that the signal obtained in s-SNOM is given by a complex combination of the different local near-field components with both linear and quadratic dependencies.[53] For a dipole antenna, it was shown that the experimental near-field distribution can deviate substantially from the numerical calculated distribution of a single near-field component, an effect that can be expected to be even more pronounced in the case of more complex structures such as the presented chiral antennas and metasurfaces. We thus apply a recently developed model for the scattering process in s-SNOM[53] (see Methods) to calculate the theoretical s-SNOM amplitude and phase images ($|E_p|$, φ_p) of the antenna near-field distribution. The model takes into account multiple scattering events between the probing tip and the antenna, which it describes in a first order approximation by (i) direct scattering of the antenna near fields by the tip into the far field (detector) and (ii) indirect scattering of the antenna near fields by the tip via the antenna itself. For comparison with the model and experiment, we also calculate the amplitude and phase of the vertical near-field component ($|E_z|$, φ_z).

We first apply our technique to image infrared Archimedean spiral antennas, which are a well-established design concept from RF antenna theory offering large bandwidth, compact dimensions, and radiation with circular polarization.[27−29] Figure 2a,b shows the topography images of a 1-turn and a 5-turn infrared Archimedean spiral antenna made of 200 nm wide and 60 nm high gold wires, separated by a 200 nm wide gap and supported on a CaF_2 substrate (see Methods for fabrication details). The near-field maps of the 1-turn antenna show similar amplitude and phase response for LCP and RCP, yielding strong fields near the antenna gap and at the arm ends (Figure 2c). Intriguingly, a dramatic difference is observed with the 5-turn antenna (Figure 2d): LCP produces a strong field concentration near the antenna gap, while no significant fields are seen on the outer part of the antenna. In contrast, for RCP illumination the fields completely extinguish at the gap and a ring-shaped field concentration is observed in a distance of 3−5 μm from the gap. These observations indicate that the length of the spiral arms decisively determines the near-field optical response to the handedness of circularly polarized light.

Remarkably, the chiral optical response of our spiral antennas operating at infrared frequencies can be explained by a directional launching of traveling waves in analogy to antenna theory.[27−29] We first consider the 5-turn antenna (Figure 2b) that exhibits an arm length of about 75 μm, which is large in terms of the wavelength (λ = 9.3 μm). This antenna can be described as an infrared two-wire transmission line,[54,55] that is wound into a spiral configuration.[27−29] In transmitting mode, a source would be connected to the transmission line terminals (the antenna gap), launching a traveling wave that propagates outward along the wires. Near the gap region, the currents on neighboring wires oscillate 180° out-of-phase and radiation is effectively canceled, as it is known from two-wire transmission lines.[29,54,55] Because of the extra half turn of the outer wire, the path difference between two neighboring wires generates an additional phase delay between the wires that increases with increasing distances from the gap. Radiation is maximum when the currents of neighboring wires become in-phase, which occurs in an annular ring of one wavelength circumference, the so-called the active region (indicated by the green dashed circle in Figures 2d). The radiated beam is circularly polarized (see Supporting Information Figure S2d), with LCP in $-z$ and RCP in $+z$ direction. Conversely, in reception mode LCP (RCP)

DOI: 10.1021/acs.nanolett.5b04416
Nano Lett. 2016, 16, 663−670

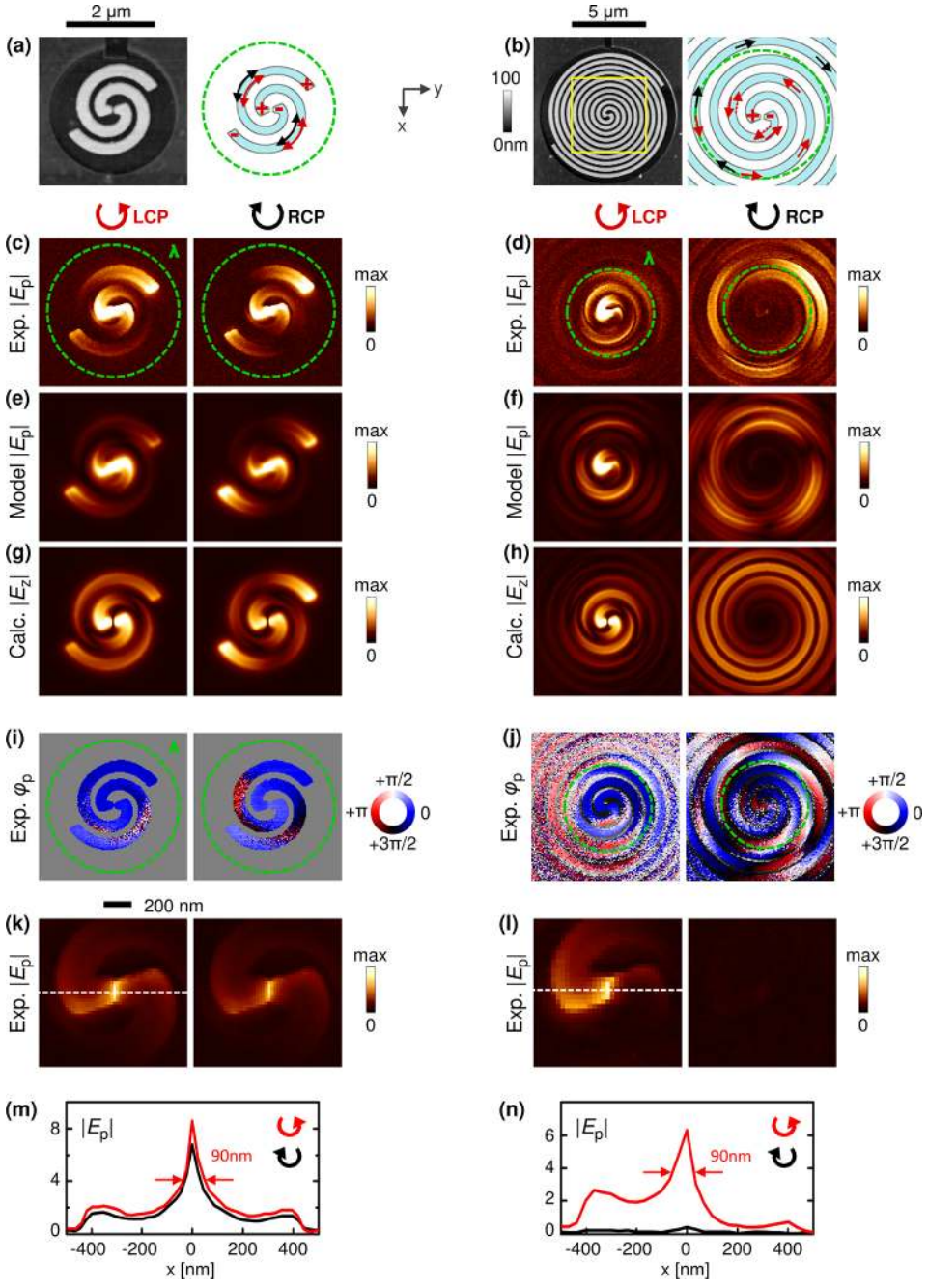

Figure 2. Nanofocusing of infrared light with circular polarization contrast in infrared Archimedean spiral antennas. (a) Left panel: Topography image of a 1-turn spiral antenna. Right panel: Illustration of a standing wave pattern on the antenna when illuminated with LCP or RCP (b). Left panel: Topography image of a 5-turn spiral antenna. Right panel: Illustration of directional wave launching at the active zone of the antenna (green dashed ring). Outward flowing currents (black arrows) excited by RCP, inward flowing currents (red arrows) excited by LCP illumination and subsequent reflection at the gap (red dashed arrows). (c,d) Experimental s-SNOM images of the antennas in (a,b). Shown is the near-field amplitude $|E_p|$ for LCP and RCP illumination. The color scale is saturated to show the antenna mode more clearly. (e,f) Modeled s-SNOM images. (g,h) Numerically calculated vertical electric field component, $|E_z|$ and φ_z. (i,j) Experimental near-field phase image, φ_p. (k,l) Digital zooms of the gap region of the near-field amplitude images shown in (c,d). (m,n) Line profiles through the nanofocus at the antenna gap, extracted at the position indicated by the dashed line in (k,l). Values of $|E_p|$ are in volts as obtained from the pseudoheterodyne module.

illumination from below in $+z$ direction launches a traveling wave at the active zone that travels inward (outward), leading to strong fields (no fields) at the antenna gap in case of the 5-turn antenna (schematic Figure 2b, right). Indeed, our near-field images confirm the directional wave launching in our infrared 5-turn spiral antenna. For RCP, we observe high amplitude signals mostly outside the green-dashed ring (Figure 2d, right), and the near-field phase image clearly shows an increasing phase along the wires as can be appreciated by the transition from blue to white to red to black color, indicating outward wave propagation (Figure 2j, right). In contrast, for LCP we observe significant amplitude signals mainly inside the green-dashed ring (Figure 2d, left) and a constant near-field phase along the wires, which we explain by an interference between the inward traveling wave and the subsequent reflected wave at the open-circuited gap (Figure 2j, left).

DOI: 10.1021/acs.nanolett.5b04416
Nano Lett. 2016, 16, 663−670

The negligible chiral optical response of the 1-turn spiral antenna (Figure 2a) can be attributed to the arm length (3.7 μm) being short in terms of the wavelength (λ = 9.3 μm). In transmitting mode, a wave launched at the gap first radiates with LCP, reflects at the outer wire ends and travels inward, radiating with a circular polarization of opposite handedness, that is, RCP. Numerical calculations (Supporting Information Figure S2b) reveal that the 1-turn antenna radiates with strongly elliptical polarization (axial ratio 5.5:1). In reception mode, the antenna thus provides only poor discrimination between LCP and RCP illumination, which explains the negligible chiral optical near-field response observed in the experiment (Figure 2c). Indeed, the phase images (Figure 2i) show constant phase on the spiral antenna (blue color) indicative of a standing wave pattern as typically observed with linear antennas.[45,53] Our images thus demonstrate that in spiral antennas, traveling waves (5-turn antenna) are the cause for a strong chiral optical response, while standing waves (1-turn antenna) are the cause for a weak chiral optical response in the near-field. As an interesting side aspect, we also observe the same, strong near-field contrast when we leave the illumination field fixed to LCP and compare the original right-wound 5-turn spiral antenna with its left-wound mirror image (Figure 3). This

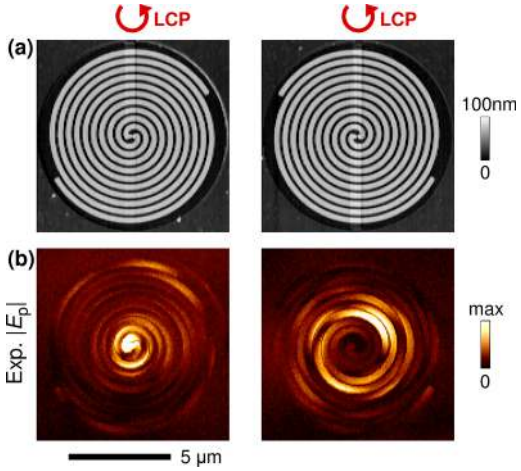

Figure 3. Chiral optical near-field contrast between a right-wound Archimedean antenna and its left-wound mirror image for the same LCP illumination. (a) Topography images. (b) Experimental near-field amplitude images of the antennas in (a) for LCP illumination.

result confirms that reversing the handedness of either the incident field or the structure itself produces the same change in the near-field response in our chiral antennas.

Closer inspection of the near-field amplitude images reveals a highly localized, intense nanofocus (hot spot) inside the antenna gap (Figure 2k,l). Interestingly, we see that the 5-turn antenna produces a hot spot only for LCP illumination, while the gap remains nearly dark for RCP (Figure 2l). The 1-turn antenna, in contrast, generates a nanofocus for both LCP and RCP (Figure 2k). We describe the polarization-selective generation of the nanofocus as the circular polarization contrast (CPC) of the antenna. To quantify it, we extracted line profiles from the near-field images in Figures 2k,l (as indicated by the dashed line), determine the near-field amplitude,$|E_p|$, at the antenna gap (x = 0) for both the LCP and RCP images and calculate the ratio CPC = $|E_p^{LCP}|/|E_p^{RCP}|$. Note that a direct and quantitative comparison between the two images is possible because only the polarization state of the illuminating beam was changed between the two image acquisitions (by rotation of the linear polarizer) whereas the detection remained unchanged. For the 5-turn antenna we obtain an impressive CPC of 16:1, which can also be appreciated by the strong peak at x = 0 for LCP (red) and the very weak peak for RCP (black line) in Figure 2n. The experimental result is confirmed by numerical calculations, predicting a CPC of 67:1 (with respect to E_{tot} at a height of 50 nm above the structures). This polarization-selective nanofocusing is a direct consequence of the inward (outward) wave launching on the antenna wires for LCP (RCP) observed in Figure 2d. We note that the experimental value can be better matched by taking into account the slight ellipticity of the illuminating beam (see Methods), then yielding a reduced CPC of 19:1 in the numerical calculations. In contrast, for the 1-turn antenna we obtain a near-unity (1.3:1) CPC (Figure 2m). We attribute this effect to the similar chiral optical response in the near field of the antenna, as discussed above.

Our results demonstrate the capability of spiral antennas to detect and enhance one specific handedness of the circular light, provided that the wire length (number of turns) is sufficiently long in terms of wavelength. We envision that this capability makes Archimedean spiral antennas a promising candidate for combining antenna-enhanced sensing with circular-polarization sensitivity in form of an integrated thin-film solution for novel spectroscopy, photodetector, and polarimetric imaging applications. For example, the spiral antenna's sensitivity to the light's handedness could be used to develop ultracompact full Stokes parameter polarimeters that do not require quarter wave plates or polarizers. Conversely, the spiral antenna's indifference to the orientation of linearly polarized illumination could simplify antenna-based sensing applications by removing the constraint of sample alignment to the (polarized) light source, such as a laser. Furthermore, spiral antennas could also find application as building blocks for constructing metasurfaces with considerable circular dichroism (CD) (up to 0.084, Supporting Information Figure S3). The CD is caused by the different scattering and absorption losses for LCP and RCP illumination. Interestingly, the strength of the CD scales with the number of turns of the antennas, and CD resonances are observed. A full clarification of the strong CD and CD resonances has to await future studies, which would go beyond the scope of this paper.

We note that the nanofocus in the antenna gap (the one discussed above) is revealed in our near-field images when recording the p-component of the scattered light, E_p (Figure 2k,l). This might be surprising and is in contrast to s-SNOM experiments with linear antennas, where detection of the p-component of the tip-scattered light typically yields a dark gap.[42,45,53] We explain the bright gap in our near-field images by a strong scattering of the antenna near fields by the tip via the antenna itself into the far field, which predominates over the direct scattering of the near fields by the tip.[53] Furthermore, the spiral antennas radiate with both s- and p-component as a result of the circular polarization of the 5-turn spiral antenna, and the tilted elliptical polarization of the 1-turn spiral antenna (Supporting Information Figure S2). Thus, the in-plane component of the field inside the gap is transferred to the p-component of the scattered field. In contrast, linear antennas radiate entirely in s-polarization normal to the antenna axis, thus the in-plane component of the field inside the gap is only contained in the s-component (assuming light detection normal

DOI: 10.1021/acs.nanolett.5b04416
Nano Lett. 2016, 16, 663−670

to the antenna axis) and consequently a dark gap is observed when the p-component is measured.[45] The employed s-SNOM model,[53] which properly accounts for the complex-valued combination of near-field components, not only confirms the bright gap but also some specific features in the experimental near-field distributions (Figures 2e,f). In more detail, the model correctly predicts the stronger field enhancement on the wire edges than on the wire center (Figures 2e), the breaks (dark spots) in the ring-shape structure (Figure 2f, RCP) and the general asymmetric nature of the amplitude distribution observed in the experiment. This detailed reproduction of the experimental images supports the validity of the s-SNOM scattering model with the spiral antennas.

We furthermore note that the Archimedean spiral geometry is also found in plasmonic lenses,[56,57] whose near fields have been imaged employing circularly polarized illumination.[58,59] These spiral lenses are based on the launching of surface plasmons on thin metal films at spiral grooves with a defined geometric phase, where a nanofocus is generated on the metal film by a radial and inward propagation of the plasmons. This mechanism is different to infrared and radiofrequency spiral antennas, where the illuminating beam excites currents in the metal wires, which travels tangentially and along the wires to produce a field concentration at the antenna gap.

To further demonstrate the wide application potential of our technique and to obtain new insights in the chiral optical near-field response of metal nanostructures, we image the chiral near-field distributions that govern circular dichroism (CD) in planar chiral metasurfaces.[11−15,17−21,24,25] To this end, we fabricated two examples: The first design consists of a single-layer array of infrared-resonant metal rosettes (Figure 4a) that exhibits very little CD.[11−15,17,20,24,25] The second design consists of an asymmetric arrangement of dipole and monopole antennas, as well as a horizontal wire acting as the ground plane for the monopole antenna (Figure 4f).[35,36] This metasurface produces strong CD due to a Fano resonance induced by capacitive coupling between the dipole and monopole antenna. The weak and strong CD of both structures can be appreciated with the calculated transmission spectra in Figure 4e,j, respectively.

With the rosette metasurface (Figure 4b), we find that the near-field images are nearly identical for LCP and RCP despite of the chiral geometry of the rosettes. In detail, our images show the same mode structure for LCP and RCP, exhibiting strong amplitude signals at the four arm ends and a node at the spiral center, and the difference in near-field amplitude is negligible. We thus observe no significant differences in the chiral optical response in the near-field of the single-layer rosette metasurface. This finding is consistent with the small to negligible CD observed in far-field studies of similar single-layer structures,[11,13−17,19,21,25] which was attributed to the missing of a significant magnetic mode.[13−15] Here, we propose an alternative explanation along the lines of antenna theory, which is motivated by the similarities of the rosettes with the 1-turn spiral antenna (Figure 2a). Both show small near-field contrast between LCP and RCP despite their obvious planar chiral geometry. Describing the rosettes as four-arm spiral antennas,[29] we notice that the rosettes' arm length (1.5 μm) is much shorter than the wavelength. Consequently, a standing wave pattern rather than a traveling wave is formed on the antenna arms, leading to a nearly linear polarization of the antenna radiation, hence the rosettes' poor discrimination between LCP and RCP illumination.

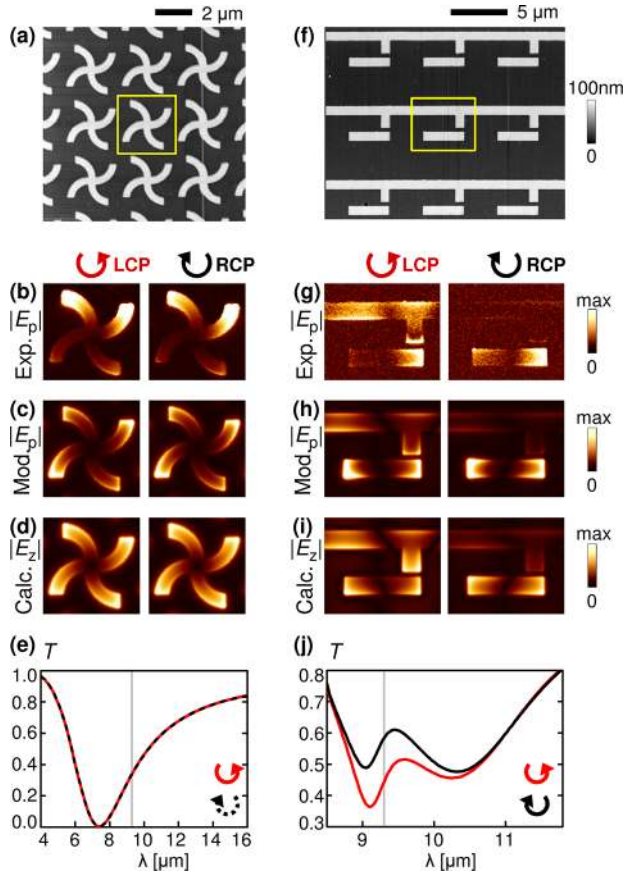

Figure 4. Chiral near-field distributions in planar chiral metasurfaces that govern the circular dichroism response in the far field. (a) Topography image of a periodic array of infrared-resonant rosettes (four arms of a 1/4-turn). (b) Experimental s-SNOM images, showing the near-field amplitude images $|E_p|$ for left-handed (LCP) and right-handed circular polarized (RCP) illumination. (c) Modeled s-SNOM images. (d) Numerically calculated vertical electric field component, $|E_z|$ and φ_z. (e) Calculated transmission spectra, T, of the rosette metasurface in (a) for LCP (red) and RCP (black dashed). (f) Topography image of an asymmetric dipole−monopole metasurface, consisting of a dipole antenna (3.58 μm × 0.79 μm) that capacitively couples to a monopole antenna (0.79 μm × 1.125 μm) connected to a horizontal wire (ground plane). (g) Experimental s-SNOM images. (h) Modeled s-SNOM images. (i) Numerically calculated vertical electric field component. (j) Calculated transmission spectra, T, of the asymmetric dipole−monopole metasurface in (f). The vertical gray line marks the imaging wavelength λ = 9.3 μm.

In contrast, the asymmetric dipole−monopole metasurface shows drastically different near-field responses between LCP and RCP illumination (Figure 4g). While the dipole antenna is always excited, we find strong fields at the monopole antenna and the horizontal wire only for LCP illumination, while the fields almost vanish for RCP. This on−off switching of the fields is caused by a Fano resonance induced by capacitive coupling between the dipole and monopole.[35,36] Because of ohmic losses in real metals, the fields observed at the monopole antenna cause additional absorption in the structure for LCP illumination, while this extra absorption is not present for RCP. The underlying physics of this finding is described in detail in ref 35. Importantly, our imaging technique reveals the different chiral near-field distributions as the cause for the CD in the asymmetric dipole−monopole metasurface. This capability we consider to be crucial for the further development of planar

DOI: 10.1021/acs.nanolett.5b04416
Nano Lett. 2016, 16, 663−670

chiral structures with strong CD (in absorption) effects. Note that the modeled s-SNOM images (Figure 4c,h) and the numerical calculation (Figure 4d,i) qualitatively confirm the experimental images for both structures (Figure 4b,g). The quantitative differences (asymmetries in the experimental images) can be attributed to the imperfect experimental conditions and the simplified description of the s-SNOM tip as a point dipole in the s-SNOM scattering model.

In conclusion, we have demonstrated, for the first time, the real-space mapping of chiral near-field distributions in planar chiral antennas and metasurfaces with s-SNOM. To this end, we have developed a new imaging modality that employs circularly polarized illumination in combination with interferometric detection. When applied to infrared Archimedean spiral antennas, our technique revealed that left- and right-handed circularly polarized light can produce strongly different near-field distributions, provided that the antenna arms are long enough in terms of the wavelength. We have shown that this effect can be exploited to selectively nanofocus incident light of only one specific handedness, which could lead to new ultracompact polarimeter applications. By imaging planar chiral metasurfaces, we have found nearly identical near-field distributions in case of single-layer rosettes while drastically different near-field distributions were observed with an asymmetric dipole−monopole metasurface, which correlates with the weak and strong circular dichroism of these structures, respectively. Our imaging technique thus paves the way for a fundamental and detailed verification of the chiral optical effects in the near field, which will play an important role for the development and optimization of planar chiral metasurfaces and their applications. Furthermore, our results indicate an interesting connection between chiral infrared antennas and radiofrequency antenna theory. The infrared spiral antenna shows a chiral optical response similar to its larger, radio-frequency counterparts, and this response can be described in terms of traveling and standing waves. This finding suggests that many RF antenna concepts are potentially suitable for building novel infrared chiral antenna and metasurfaces, which is certainly worth to be explored further in the future.

Methods. *Sample Fabrication.* The metal nanostructures were fabricated by focused ion beam (FIB) milling of a 60 nm thick thermally evaporated Au layer on a CaF_2 substrate using a three-step milling process.[60] In a first step, we removed the metal around the nanostructures with a high-current setting (double pass, 500 pA). Only a thin metal bridge remained after milling that still connected electrically the structures with the grounded gold film. This measure avoided charging of the sample and subsequent beam deflection during the following milling steps. In a second step, we milled the nanostructure contour and features such as gaps at a lower current setting of 30−100 pA (double pass). In a third step, we removed the metal bridges and obtained the final structure. We note that in case of the spiral antennas, the gold wires are 200 nm wide with a 200 nm gap between them, while in the topography images in Figure 2, the wires appear to be wider while the gaps appear narrower than 200 nm, which is due to the finite size of the s-SNOM tip.

Near-Field Microscope Setup. To map the near-field distributions in chiral metal nanostructures, we apply interferometric s-SNOM.[42−52] It offers an excellent spatial resolution in the 10 nm range independently of the wavelength, operates in a wide spectral range including visible, infrared, and terahertz frequencies, and provides access to both the local near-field amplitude and phase, which enables the unambiguous recognition of localized antenna modes and propagating waveguide modes. Our s-SNOM setup (Figure 1) is based on an atomic force microscope where commercial silicon tips (NanoWord, Arrow-NCR-50) were used to locally scatter the near-fields on the sample surface. The sample and tip were illuminated from below at normal incidence with a weakly focused CO_2 laser beam at wavelength λ = 9.3 μm (transmission-mode s-SNOM),[42,43] thus ensuring homogeneous illumination without phase-retardation effects of an area larger than the structures investigated in this work. We introduced a linear polarizer P (www.lasnix.com, model LP01) and a phase retarding mirror PMR (Rocky Mountain Instruments) into the path of the illuminating beam to generate LCP and RCP light. Note that here we define LCP and RCP as a wave propagating in +z direction with a counterclockwise and clockwise rotation of the electric field vector in the (x,y) plane (from the point of view of the receiver), respectively. Switching between LCP and RCP was achieved by rotating the polarizer P. The design wavelength of the PMR is 9.3 μm, and we characterized the axial ratio of RCP and LCP to be 1.17:1 at this wavelength, as obtained by registering the light transmitted through a linear analyzer upon one rotation with an infrared detector. This slight ellipticity we explain by the fabrication tolerances of the PMR element, specified by the manufacturer to be 90° ± 6° for the introduced phase shift between the orthogonal components of the circular polarization. We collected the light scattered from the tip and the sample with a parabolic mirror in +x-direction at an angle of 60° from the surface normal and superimposed it with a p-polarized phase-modulated reference beam at the infrared detector. Background contributions could be fully suppressed by vertical tip oscillation at a frequency Ω = 250 kHz (tapping-mode AFM) and by subsequent higher harmonic demodulation of the detector signal at 3Ω. Using a pseudoheterodyne detection scheme,[61] we obtained the amplitude and phase of the p-component of the scattered light, denoted as $|E_p|$ and φ_p.

Numerical Calculations and Modeled s-SNOM Images. We numerically calculated the electric near-field distributions of the presented metal nanostructures using a commercial finite-difference time-domain (FDTD) software package (FDTD Solutions, Lumerical). We assumed an illuminating plane wave from below at normal incidence at a free-space wavelength of 9.3 μm, a dielectric value for gold of $\epsilon_{Au} = -2598 + 1157i$ according to Palik and for the CaF_2 substrate of $\epsilon_{CaF_2} = 1.74$. The electric field was calculated at a height of 50 nm above the metal nanostructures, $\mathbf{E}_{inc}(x, y)$. In the manuscript, we plotted the z-component $E_z(x, y)$ to visualize the near-field distribution in the vicinity of the nanostructures. The modeled s-SNOM images were calculated using a recently introduced model that takes into account multiple scattering events between the tip and the sample, as well as the combination of the different near-field components in the s-SNOM signal, depending on the illumination and detection conditions.[53] To this end, we first calculated the electric field at a height of 50 nm above the metal nanostructures, $\mathbf{E}_{inc}(x, y)$, for sample illumination from below with either LCP or RCP. We then performed an additional numerical simulation of the electric fields at the same height above the metal nanostructures, $\mathbf{E}_{virt}(x, y)$, where we assumed a p-polarized plane-wave illumination incident on the sample from the same direction as the collection of the scattered light was taking place, that is, + x-direction at an angle of 60° to the

DOI: 10.1021/acs.nanolett.5b04416
Nano Lett. 2016, 16, 663−670

surface normal. For each illumination polarization (LCP, RCP), we then calculated the scattered field $\mathbf{E}_p(x, y)$ according to

$$\mathbf{E}_p(x, y) \propto \mathbf{E}_{virt}(x, y)\cdot\alpha^T\cdot\mathbf{E}_{inc}(x, y) \quad (1)$$

We assumed a diagonal scattering tensor of the tip, α^T, where we choose $\alpha_x^T = \alpha_y^T = \alpha_z^T = 1$ to obtain best agreement with the experimental s-SNOM maps (Figures 2), and $\alpha_x^T = \alpha_y^T = 1$ and $\alpha_z^T = 3$ in Figure 4.

■ ASSOCIATED CONTENT

Supporting Information

The Supporting Information is available free of charge on the ACS Publications website at DOI: 10.1021/acs.nanolett.5b04416.

Complete experimental and simulated data sets of the 1-turn and 5-turn spiral antenna shown in Figure 2. Calculated radiation characteristics of the infrared 1-turn and 5-turn Archimedean spiral antennas shown in Figure 2. Circular dichroism (CD) and CD resonances in single-layer metasurfaces consisting of infrared spiral antennas. (PDF)

■ AUTHOR INFORMATION

Corresponding Author

*E-mail: r.hillenbrand@nanogune.eu.

Author Contributions

Authors M.S. and P.S. contributed equally to this work.

Notes

The authors declare the following competing financial interest(s): R.H. is co-founder of Neaspec GmbH, a company producing scattering-type scanning near-field optical microscope systems such as the one used in this study. All other authors declare no competing financial interests.

■ ACKNOWLEDGMENTS

The authors acknowledge support by the European Union through ERC starting grants (TERATOMO Grant 258461); the Spanish Ministry of Economy and Competitiveness (National Projects MAT2012-36580, MAT2012-37638, and FIS2013-41184P) and from the Basque Government (Project PI2011-1 and project ETORTEK nanogune'14). G.S. acknowledges support by the Office of Naval Research (Grant N00014-13-1-0837).

■ REFERENCES

(1) Novotny, L.; van Hulst, N. *Nat. Photonics* **2011**, *5*, 83−90.
(2) Soukoulis, C. M.; Wegener, M. *Nat. Photonics* **2011**, *5*, 523−530.
(3) Kildishev, A. V.; Boltasseva, A.; Shalaev, V. M. *Science* **2013**, *339*, 1232009.
(4) Xu, H.; Bjerneld, E. J.; Käll, M.; Börjesson, L. *Phys. Rev. Lett.* **1999**, *83*, 4357−4360.
(5) Neubrech, F.; Pucci, A.; Cornelius, T. W.; Karim, S.; Garcia-Etxarri, A.; Aizpurua, J. *Phys. Rev. Lett.* **2008**, *101*, 157403.
(6) Tang, L.; Kocabas, S. E.; Latif, S.; Okyay, A. K.; Ly-Gagnon, D. S.; Saraswat, K. C.; Miller, D. A. B. *Nat. Photonics* **2008**, *2*, 226−229.
(7) Pendry, J. B. *Phys. Rev. Lett.* **2000**, *85*, 3966−3969.
(8) Shalaev, V. M. *Nat. Photonics* **2007**, *1*, 41−48.
(9) Landy, N. I.; Sajuyigbe, S.; Mock, J. J.; Smith, D. R.; Padilla, W. J. *Phys. Rev. Lett.* **2008**, *100*, 207402.
(10) Valev, V. K.; Baumberg, J. J.; Sibilia, C.; Verbiest, T. *Adv. Mater.* **2013**, *25*, 2517−2534.
(11) Papakostas, A.; Potts, A.; Bagnall, D. M.; Prosvirnin, S. L.; Coles, H. J.; Zheludev, N. I. *Phys. Rev. Lett.* **2003**, *90*, 107404.
(12) Vallius, T.; Jefimovs, K.; Turunen, J.; Vahimaa, P.; Svirko, Y. *Appl. Phys. Lett.* **2003**, *83*, 234−236.
(13) Plum, E.; Fedotov, V. A.; Schwanecke, A. S.; Zheludev, N. I.; Chen, Y. *Appl. Phys. Lett.* **2007**, *90*, 223113.
(14) Decker, M.; Klein, M. W.; Wegener, M.; Linden, S. *Opt. Lett.* **2007**, *32*, 856−858.
(15) Plum, E.; Zhou, J.; Dong, J.; Fedotov, V. A.; Koschny, T.; Soukoulis, C. M.; Zheludev, N. I. *Phys. Rev. B: Condens. Matter Mater. Phys.* **2009**, *79*, 035407.
(16) Gansel, J. K.; Thiel, M.; Rill, M. S.; Decker, M.; Bade, K.; Saile, V.; von Freymann, G.; Linden, S.; Wegener, M. *Science* **2009**, *325*, 1513−1515.
(17) Wang, B.; Zhou, J.; Koschny, T.; Kafesaki, M.; Soukoulis, C. M. *J. Opt. A: Pure Appl. Opt.* **2009**, *11*, 114003.
(18) Liu, N.; Liu, H.; Zhu, S.; Giessen, H. *Nat. Photonics* **2009**, *3*, 157−162.
(19) Zhang, S.; Park, Y.-S.; Li, J.; Lu, X.; Zhang, W.; Zhang, X. *Phys. Rev. Lett.* **2009**, *102*, 023901.
(20) Hendry, E.; Carpy, T.; Johnston, J.; Popland, M.; Mikhaylovskiy, R. V.; Lapthorn, A. J.; Kelly, S. M.; Barron, L. D.; Gadegaard, N.; Kadodwala, M. *Nat. Nanotechnol.* **2010**, *5*, 783−787.
(21) Zhao, Y.; Belkin, M. A.; Alù, A. *Nat. Commun.* **2012**, *3*, 870.
(22) Wu, C.; Arju, N.; Kelp, G.; Fan, J. A.; Dominguez, J.; Gonzales, E.; Tutuc, E.; Brener, I.; Shvets, G. *Nat. Commun.* **2014**, *5*, 3892.
(23) Pendry, J. B. *Science* **2004**, *306*, 1353−1355.
(24) Kwon, D.-H.; Werner, P. L.; Werner, D. H. *Opt. Express* **2008**, *16*, 11802−11807.
(25) Schäferling, M.; Dregely, D.; Hentschel, M.; Giessen, H. *Phys. Rev. X* **2012**, *2*, 031010.
(26) Tang, Y.; Cohen, A. E. *Phys. Rev. Lett.* **2010**, *104*, 163901.
(27) Dyson, J. *IRE Trans. Antennas Propag.* **1959**, *7*, 181−187.
(28) Kaiser, J. *IRE Trans. Antennas Propag.* **1960**, *8*, 312−323.
(29) Balanis, C. A. *Antenna Theory*; John Wiley & Sons, Inc.: Hoboken, NJ, 2005.
(30) Grossman, E. N.; Sauvageau, J. E.; McDonald, D. G. *Appl. Phys. Lett.* **1991**, *59*, 3225−3227.
(31) Fumeaux, C.; Boreman, G. D.; Herrmann, W.; Rothuizen, H.; Kneubühl, F. K. *Appl. Opt.* **1997**, *36*, 6485−6490.
(32) González, F. J.; Boreman, G. D. *Infrared Phys. Technol.* **2005**, *46*, 418−428.
(33) Ziegler, J. I.; Haglund, R. F. *Nano Lett.* **2010**, *10*, 3013−3018.
(34) Zhao, Y.; Alù, A. *Phys. Rev. B: Condens. Matter Mater. Phys.* **2011**, *84*, 205428.
(35) Khanikaev, A. B.; Arju, N.; Fan, Z.; Purtseladze, D.; Lu, F.; Lee, J.; Sarriugarte, P.; Schnell, M.; Hillenbrand, R.; Belkin, M.; et al. Unpublished work, 2015.
(36) Khanikaev, A. B.; Mousavi, S. H.; Wu, C.; Dabidian, N.; Alici, K. B.; Shvets, G. *Opt. Commun.* **2012**, *285*, 3423−3427.
(37) Fedotov, V. A.; Schwanecke, A. S.; Zheludev, N. I.; Khardikov, V. V.; Prosvirnin, S. L. *Nano Lett.* **2007**, *7*, 1996−1999.
(38) Arju, N.; Ma, T.; Khanikaev, A.; Purtseladze, D.; Shvets, G. *Phys. Rev. Lett.* **2015**, *114*, 237403.
(39) Takahashi, S.; Potts, A.; Bagnall, D.; Zheludev, N. I.; Zayats, A. V. *Opt. Commun.* **2005**, *255*, 91−96.
(40) Narushima, T.; Okamoto, H. *Phys. Chem. Chem. Phys.* **2013**, *15*, 13805−13809.
(41) Narushima, T.; Okamoto, H. *J. Phys. Chem. C* **2013**, *117*, 23964−23969.
(42) Schnell, M.; Garcia-Etxarri, A.; Huber, A. J.; Crozier, K. B.; Aizpurua, J.; Hillenbrand, R. *Nat. Photonics* **2009**, *3*, 287−291.
(43) Schnell, M.; Garcia-Etxarri, A.; Huber, A. J.; Crozier, K. B.; Borisov, A. G.; Aizpurua, J.; Hillenbrand, R. *J. Phys. Chem. C* **2010**, *114*, 7341−7345.
(44) Schnell, M.; Garcia-Etxarri, A.; Alkorta, J.; Aizpurua, J.; Hillenbrand, R. *Nano Lett.* **2010**, *10*, 3524−3528.
(45) Alonso-González, P.; Albella, P.; Schnell, M.; Chen, J.; Huth, F.; Garcia-Etxarri, A.; Casanova, F.; Golmar, F.; Arzubiaga, L.; Hueso, L. E.; et al. *Nat. Commun.* **2012**, *3*, 684.

DOI: 10.1021/acs.nanolett.5b04416
Nano Lett. 2016, 16, 663−670

(46) Keilmann, F.; Hillenbrand, R. *Philos. Trans. R. Soc., A* **2004**, *362*, 787−805.
(47) Olmon, R. L.; Krenz, P. M.; Jones, A. C.; Boreman, G. D.; Raschke, M. B. *Opt. Express* **2008**, *16*, 20295−20305.
(48) Esteban, R.; Vogelgesang, R.; Dorfmüller, J.; Dmitriev, A.; Rockstuhl, C.; Etrich, C.; Kern, K. *Nano Lett.* **2008**, *8*, 3155−3159.
(49) Kim, Z. H.; Leone, S. R. *Opt. Express* **2008**, *16*, 1733−1741.
(50) Rang, M.; Jones, A. C.; Zhou, F.; Li, Z.-Y.; Wiley, B. J.; Xia, Y.; Raschke, M. B. *Nano Lett.* **2008**, *8*, 3357−3363.
(51) Kim, D.-S.; Heo, J.; Ahn, S.-H.; Han, S. W.; Yun, W. S.; Kim, Z. H. *Nano Lett.* **2009**, *9*, 3619−3625.
(52) Tucker, E.; D'Archangel, J.; Raschke, M. B.; Boreman, G. *J. Appl. Phys.* **2012**, *116*, 044903.
(53) Neuman, T.; Alonso-González, P.; Garcia-Etxarri, A.; Schnell, M.; Hillenbrand, R.; Aizpurua, J. *Laser Photonics Rev.* **2015**, *9*, 637−649.
(54) Schnell, M.; Alonso Gonzalez, P.; Arzubiaga, L.; Casanova, F.; Hueso, L. E.; Chuvilin, A.; Hillenbrand, R. *Nat. Photonics* **2011**, *5*, 283−287.
(55) Krenz, P. M.; Olmon, R. L.; Lail, B. A.; Raschke, M. B.; Boreman, G. D. *Opt. Express* **2010**, *18*, 21678−21686.
(56) Ohno, T.; Miyanishi, S. *Opt. Express* **2006**, *14*, 6285−6290.
(57) Drezet, A.; Genet, C.; Laluet, J.-Y.; Ebbesen, T. W. *Opt. Express* **2008**, *16*, 12559−12570.
(58) Gorodetski, Y.; Niv, A.; Kleiner, V.; Hasman, E. *Phys. Rev. Lett.* **2008**, *101*, 043903.
(59) Chen, W.; Abeysinghe, D. C.; Nelson, R. L.; Zhan, Q. *Nano Lett.* **2010**, *10*, 2075−2079.
(60) Sarriugarte, P.; Schnell, M.; Chuvilin, A.; Hillenbrand, R. *ACS Photonics* **2014**, *1*, 604−611.
(61) Ocelic, N.; Huber, A.; Hillenbrand, R. *Appl. Phys. Lett.* **2006**, *89*, 101124.

DOI: 10.1021/acs.nanolett.5b04416
Nano Lett. 2016, 16, 663−670